

promoting access to White Rose research papers



Universities of Leeds, Sheffield and York
<http://eprints.whiterose.ac.uk/>

This is an author produced version of a paper published in **Geophysical Journal International**

White Rose Research Online URL for this paper:

<http://eprints.whiterose.ac.uk/id/eprint/77392>

Paper:

Angus, DA, Wilson, DC, Sandvol, E and Ni, JF (2006) *Lithospheric structure of the Arabian and Eurasian collision zone in eastern Turkey from S-wave receiver functions*. *Geophysical Journal International*, 166 (3). 1335 – 1346

<http://dx.doi.org/10.1111/j.1365-246X.2006.03070.x>

Lithospheric Structure of the Arabian and Eurasian Collision Zone in Eastern Turkey from S–wave Receiver Functions

D.A. Angus¹ *, David C. Wilson², E. Sandvol³ & J.F. Ni¹

¹*Department of Physics, New Mexico State University, Las Cruces, NM, USA, 88003-8001*

²*Jackson School of Geosciences, University of Texas at Austin, Austin, TX, USA*

³*Department of Geological Sciences, University of Missouri, Columbia, MO, USA*

Submitted to GJI: Fall 2005

SUMMARY

Crustal and upper–mantle seismic discontinuities beneath eastern Turkey are imaged using teleseismic S–to–P converted phases. Three crustal phases are observed: the Moho with depth ranging between 30 and 55 km, indicating variable tectonic regimes within this continental collision zone; an upper–crustal discontinuity at approximately 10 km depth; and various crustal low–velocity zones, possibly associated with recent Quaternary volcanism. Imaging of the upper mantle is complicated by the three–dimensional geometry of the region, in particular due to the Bitlis–Zagros suture zone. However, several upper–mantle S–to–P converted phase are identified as being the signature of the lithosphere–asthenosphere boundary (LAB). The inferred LAB for the Eastern Anatolian Accretionary Complex indicates that eastern Turkey has an anomalously thin (between ~ 60 and 80 km) lithosphere which is consistent with an oceanic slab detachment model. The observed LAB phases for the Arabian shield and Iranian plateau indicate that lithospheric thickness for these stable regions is on the order of 100 to 125 km thick, which is typical of continental margins.

Key words: crust, eastern Turkey, lithosphere–asthenosphere boundary, seismic discontinuity, S–wave receiver function.

1 INTRODUCTION

The Anatolian plateau in eastern Turkey is a region in the early stages of continent–continent collision and so provides a unique natural laboratory to study the early development of continental plateau. Located within the Alpine–Himalayan fold–thrust fault belt (see Figure 1), the Anatolian plateau is geologically very complex, with over half of the surface area covered with late Cenozoic volcanics of diverse composition (Pearce et al., 1990; Keskin, 2003). The plateau is also seismically active and is dissected by numerous seismogenic faults predominantly of strike–slip motion.

The deformation style in the Anatolian plateau differs from east to west, with translational movement and transcompressional deformation in the east and, in the west, coherent plate motion involving the westward motion and counterclockwise rotation of the Anatolian plate with little or no internal deformation in the central Anatolian plate (Reilinger et al., 1997a,b; Jiménez–Munt et al., 2003; Türkelli et al., 2003). Focal mechanism studies indicate that collision is accommodated by strike–slip faults, suggesting that escape tectonics dominates and that thrust faulting and other compressive features, although still active, are of lesser importance (Örgülü et al., 2003). Reilinger et al. (1997a) suggest that the differing deformation styles in the east and west result from differing plate boundary conditions. The ‘free’ boundary of the Hellenic arc in the west assists in the westward motion of the Anatolian plate, whereas, in the east, the Eurasian continent and the oceanic lithosphere of the Black and Caspian Seas provide a resistant boundary to northward and eastward motion. This resistance leads to deformation in eastern Turkey that is accommodated by distributed strike–slip faulting and crustal shortening.

*Now at: Department of Earth Sciences, University of Bristol, Bristol, UK

The crust of eastern Turkey is hot and weak (e.g., Reilinger et al., 1997a) and composed of crustal slivers that are in relative motion to one another. In some respect, the Anatolian plateau is similar to the crustal mosaic of central Iran (e.g., Şengör & Kidd, 1979). However, unlike Iran, there is no well-developed fold and thrust belt in front of the Bitlis suture similar to the Zagros. This may reflect lateral variations in the structure and rheology of the leading edge of the colliding Arabian continental plate and/or variations in the Iranian versus the Turkish terrains and their ability to partially escape from the advancing Arabia.

P-wave receiver function studies have suggested that the crustal thickness in eastern Turkey is, on average, less than 45 km (Çakir et al., 2003; Zor et al., 2003; Çakir et al., 2004). The crustal thickness varies from about 38 km in the Arabian foreland in southern Turkey to about 50 km farther north in the Pontides mountain range that extends along the Black Sea. The region is seismically very active, with the majority of earthquakes correlating well with mapped faults. However, there are many events that occur in areas where no surface faults are mapped (Türkelli et al., 2003). The vast majority of the earthquakes occur within the upper 25 km of the crust, and no sub-crustal earthquakes occur anywhere in the region. These crustal thickness estimates suggest that there is very little underthrusting of the Arabian plate beneath eastern Turkey. Sandvol et al. (2003b) correlate large shear-wave splitting delay times with regions of low Pn velocity and find that the fast symmetry axes are not consistent with surface or crustal deformation. The anisotropy is interpreted to be mostly asthenospheric related, where the fast axis is related to the vector difference between the lithospheric and mantle flow velocity vectors.

Investigation of the mantle lithosphere from Pn tomography (Hearn & Ni, 1994; Al-Lazki et al., 2003; Al-Damegh et al., 2004), Sn attenuation (Rodgers et al., 1997; Gök et al., 2003; Al-Damegh et al., 2004) and surface waveform tomography (Maggi & Priestley, 2005) studies indicate that the Anatolian lithospheric mantle is seismically very slow. These independent measurements indicate that the uppermost mantle is partially molten and the asthenospheric material is in close proximity to the base of the crust. Recent tomography results (Sandvol & Zor, 2004) indicate that the ultra-low Pn velocity zone is also underlain by a slightly low velocity in the upper mantle beneath the northern Arabian plate and the easternmost portion of the Anatolian plate. Furthermore, high Bouguer gravity anomalies support the presence of asthenospheric material underlying the Moho in this region (Ates et al., 1999; Barazangi et al., 2005).

Crustal and upper-mantle processes at the convergent boundary between the Arabian and Eurasian plates in eastern Turkey and adjacent regions have received extensive attention because the Eastern Anatolian Accretionary Complex (EAAC), a subduction-accretion prism of Cretaceous to early Oligocene age, is being converted into continent through A-type granite magmatism and felsic and intermediate volcanism (e.g., Şengör & Natal, 1996; Şengör et al., 2003). However, the thickness of the lithosphere and the spatial extent of the crustal low velocity layers and their relationship to the upper-mantle low velocity zones remain poorly known; hence it remains difficult to differentiate between competing geodynamic models for this region. In this paper, the S-wave receiver function method is applied to digitally recorded broadband seismograms from the Eastern Turkey Seismic Experiment (ETSE) to investigate the crust and upper mantle structure of this continent-continent collision zone. Images of crustal and upper-mantle seismic discontinuities are presented for various east-west and north-south vertical profiles, which sample portions of the Arabian shield, the Anatolian and Iranian block, the EAAC and the Lesser Caucasus.

2 REVIEW OF TECTONIC HISTORY

The complex geology of the Anatolian region of eastern Turkey is a product of the collision of two continents, Gondwanaland in the south and Eurasia in the north, where continental fragments of varied geologic history have been accreted to Eurasia throughout the Mesozoic and Cenozoic time (Barazangi et al., 2005). The Neo Tethys was subducted beneath the southern margin of Eurasia and was completely consumed during the late Paleocene along the Pontide arc (e.g. Şengör & Yilmaz, 1981; Bozkurt & Mittwede, 2001). However, a segment of the southern oceanic branch of the Neo Tethys attached to the Arabian plate continued its northward subduction beneath eastern Turkey through the middle Miocene (e.g., Yilmaz, 1993, Figure 7). The upper plate, back-arc region is mostly the site of the EAAC, which was associated with the Pontide subduction system (e.g., Şengör et al., 2003). The final continental collision and suturing of Arabia with the Turkish terrains in the middle Miocene resulted in the complete annihilation of subduction of the Neo Tethys ocean in eastern Turkey (e.g., Şengör & Kidd, 1979; Dewey et al., 1986; Yilmaz, 1993; Bozkurt & Mittwede, 2001; Şengör et al., 2003). Subsequent to this collision a major episode of widespread volcanism with varied and complex composition affected most of the eastern Anatolian region starting at about 11 Ma (e.g., Keskin, 2003).

A recent model has been suggested that explains both the geologic and geophysical observations in the region (Şengör et al., 2003; Keskin, 2003). This model involves the breakoff of a northward subducted slab that allowed hot, partially molten asthenospheric material to be in close proximity to the bottom of the crust. This could explain the extensive melting, the initiation of collisional volcanism and the relatively rapid regional uplift to form the 2 km high east Anatolian plateau. Both Şengör et al. (2003) and Keskin (2003) propose that the detached slab is that which descended beneath the Pontide arc system (i.e., the northern oceanic branch of the Neo Tethys). Barazangi et al. (2005) propose an alternative scenario where the detached slab is the southern oceanic Neo Tethys that was descending shallowly beneath the Bitlis arc system (i.e., the

oceanic segment of the Arabian lithosphere). This slab breakoff and the subsequent sinking of the detached slab into the upper mantle is the main cause of the widespread episode of volcanism within Anatolia and the dynamically supported uplift of the east Anatolian plateau.

The latest major tectonic events in the late Cenozoic geologic evolution of Anatolia are the development of the North Anatolian fault, the East Anatolian fault and the Dead Sea fault. The resulting northward relative differential plate motion between Arabia and Africa has accelerated the convergence of Arabia relative to Eurasia in the early Pliocene time (e.g., Bozkurt, 2001). This apparently led to the development of the North Anatolian fault in the early Pliocene and subsequently the East Anatolian fault (e.g., Bozkurt, 2001; Koçyiğit et al., 2001). The northernmost segment of the Dead Sea fault joined the East Anatolian fault in the Maras region of southern Turkey to form the Anatolian–Arabian–African triple junction (e.g., Karig & Kozlu, 1990). The development of these fault systems provided the mechanism for the tectonic escape of the Anatolian crustal block toward the Aegean arc system (e.g., Burke & Şengör, 1987). With the escape westward of the Anatolian plateau, the EAAC absorbed the relative north–south compression through internal deformation and shortening.

Studies of collision–related volcanics indicate that deformation involved detachment of a thermal boundary layer via delamination, where initiation of volcanism around 11 Ma coincided with rapid uplift of the Anatolian plateau (Şengör et al., 2003; Keskin, 2003). Areas of very thin mantle lithosphere appear to coincide with the lateral extent of the EAAC (Keskin, 2003; Şengör et al., 2003). Furthermore, the location of mantle low–velocity zones is consistent with the location of Quaternary volcanics (Sandvol, 2004).

3 DATA AND METHOD

The ETSE array was designed to study the crust and upper mantle beneath Eastern Turkey (Sandvol et al., 2003a) and consisted of 29 broadband PASSCAL stations deployed over a period of roughly 22 months between November, 1999 and July, 2001 (see Figure 2). The stations were equipped with STS–2 sensors and one Guralp CMG–3T sensor (station EZRM). Two additional permanent broadband stations were also used in this study; station GNI from the Global Seismograph Network (GSN–IRIS/USGS) and station MALT from the GEOFON (GFZ–Potsdam) Network.

The receiver function method, which utilises deconvolution to minimise instrument response as well as source and propagation–path effects, is commonly applied to emphasise vertically to sub–vertically propagating converted phases to delineate seismic discontinuities (e.g., Jordan & Frazer, 1975; Bock, 1988, 1991). There are a variety of receiver function techniques and the methodological differences depend not only on the actual converted mode used (i.e., P–to–S versus S–to–P converted waves), but also on the form of component rotation in the deconvolution process. The P–receiver function is the most commonly used approach for imaging crustal and mantle discontinuities primarily for two reasons; the P–wave arrival is generally easy to identify and the deconvolution of instrument response and source/path effects is relatively robust with respect to the form of component rotation used in the deconvolution process. One major drawback of the P–wave receiver function approach is that crustal and upper–mantle conversions are contaminated by primary P–wave crustal multiples. These multiples can have larger amplitude than the direct converted phases and tend to obscure arrivals from deeper lithospheric discontinuities, such as the lithospheric–asthenospheric boundary (Farra & Vinnik, 2000). Furthermore, crustal multiples can be particularly troublesome for stations located over deep sedimentary basins (Wilson et al., 2003). One of the primary advantages of the S–wave receiver function over the P–wave receiver function is that it tends not to suffer from contamination by multiply–reflected primary S–wave energy since the converted S–to–P phases travel faster, and therefore arrive before the primary S–wave energy. Because of this, the S–wave receiver function may be more useful in imaging lower–crustal and upper–mantle discontinuities, such as the LAB (e.g., Li et al., 2004; Kumar et al., 2005). However, with respect to P–wave receiver functions, the S–wave receiver function is lower in frequency (which limits the vertical resolution of seismic discontinuities) and requires more restrictive event criteria (Bock & Kind, 1991; Wilson et al., in press).

A total of 81 events with epicentral distances between 60° and 75° , depths ≤ 300 km and magnitude (mb) ≥ 5.8 were used (Figure 3). Wilson et al. (in press) show that by restricting events to within this epicentral distance and depth range, true S–wave receiver function phases can be isolated from interfering (or parasitic) P–wave energy (e.g., pPPP and sPPP phases). The data are filtered between 1/40 and 1 Hz and the waveforms are rotated into the theoretical ray coordinates using a 1–D velocity model generated from the Rayleigh–wave tomography study of Sandvol (in prep.). In ray coordinates, the P component is along the direction of propagation, the Sv component is perpendicular to the P component within the vertical plane and the tangential (or Sh) component is normal to the vertical plane defined by the P and Sv components. Although the true velocity structure will differ (to varying degrees) from that of the 1D velocity model used in the processing, any bias due to error or noise introduced from improper rotation will likely be reduced through signal stacking. This is because each imaging bin contains multiple rays coming from different angles and azimuths and so any rotational error will be different for each ray and will likely be reduced when stacked. In previous studies, we had experimented with other procedures for component rotation (e.g., applying polarization filters) and found that, for our S–wave receiver function approach, more stable results were obtained when using theoretical incidence angles. To estimate the source, a 15 second time window is applied

around the direct S-wave arrival on the Sv component using a 5 second Hamming taper. Deconvolution is performed in the frequency domain and an optimum water level is selected based on a criterion which minimises the second-order derivative of the receiver function (i.e., trade off between fitting the data and producing a receiver function with minimal ringing). To filter out signals with weak Sv component (and thus weak S-to-P conversions), receiver functions were evaluated only for raw S-wave signals with a signal to noise ratio greater than 1.2:1 on the Sv component.

For receiver functions from multiple stations, two-dimensional cross sections (or three-dimensional mappings) of seismic discontinuities can be produced using the exploration seismic analog of the common conversion point (CCP) image (e.g., Dueker & Sheehan, 1998). The CCP image is created by first back-projecting the recorded signal along the theoretical ray path and then binning the data into lateral and depth bins. The depth cross section is then calculated by taking the mean sample value in each bin. When significant lateral structural heterogeneity exists, the mapping may be a poor representation of the true Earth structure due to diffractive effects. For such scenarios, the migration of the scattered phases can be applied to improve the positioning of discontinuities (e.g., Bostock & Rondenay, 1999; Wilson & Aster, 2005). However, even in such scenarios, the CCP imaging method provides an adequate first-order image of crustal and upper-mantle discontinuities.

A total of 921 S-wave receiver functions were used for CCP imaging. Theoretical ray paths for back projecting the deconvolved wavefield into depth and lateral bins were calculated using the 1-D Rayleigh-wave velocity model of Sandvol (in prep.). Since the station spacing for the ETSE array ranged between 50 and 75 km, receiver function amplitudes were stacked along ray paths with a lateral bin radius of 50 km. Stacked receiver function amplitudes within a given bin were scaled by the semblance of amplitudes within the bin to help mitigate the effects of possible high receiver function noise levels. In other words, at a given depth an imaging bin is a weighted average of all receiver function rays which pass within 50 km laterally of that imaging point.

It is important to note that gaps in the following receiver function plots (e.g., bottom-left and top-right portions of figures) do not indicate missing crustal or upper-mantle structure. These gaps are due to the lack of ray coverage since the events used in the receiver function analysis come from east of the array.

4 DISCUSSION OF RECEIVER FUNCTIONS

4.1 East-west profiles

Figure 4 displays CCP images of four east-west vertical slices at latitudes 37°, 38°, 39° and 40° N. Two crustal phases are clearly visible; the Moho, with depth varying between 30 and 45 km and an upper-crustal discontinuity (UCD) at roughly 10 km depth. In section 37° N, the Moho depth of the northern margin of the Arabian plate (or shield) is approximately 40 km and is consistent with the P-wave receiver function and wide-angle controlled-source reflection study of Mohsen et al. (2005) across the Dead Sea Transform further south. In the remaining sections, the Moho depth increases from approximately 30 km in the west up to 45 km or more in the east. The thickest crust (~ 48 km) is found beneath the central EAAC between 41° and 42° E. The UCD is consistent throughout all sections, though there are regions where this phase is weak or non-existent. The fluctuation of the UCD depth appears to be independent of the Moho depth and this would suggest that the UCD represents a boundary between differing deformation styles, where brittle faulting is occurring in the upper crust and ductile flow is occurring in the lower crust (e.g., Keskin, 2005). In the Zagros mountain belt, Hatzfeld et al. (2003) invert P and S traveltimes from local earthquakes and observe a thick sedimentary layer (~ 11 km and $V_p \sim 4.70$ km/s) overlying a thick upper crystalline crust (~ 8 km and $V_p \sim 5.85$ km/s). Therefore, the UCD may be interpreted as a boundary associated with contrasting velocities of crystalline basement below and thick volcano-sedimentary successions above. The thick crust beneath the EAAC suggests that the upper crust is being thickened by extensive magma generation (Keskin, 2005) as well as thrust and strike-slip faulting, where as the lower crust thickened by crustal flow processes.

Another interesting feature seen in section 39° N is the several negative phases at approximately 25 km depth centred at longitude 42° E. The discontinuity associated with this negative phase is referred to as a crustal low velocity zone (CLVZ) and is observed below recent (Quaternary) volcanic centres near the city of Van in the EAAC. The CLVZ most likely represents a pocket of partial melt in the middle crust, which is related to the magmatic ascension process for these volcanoes (e.g., Keskin et al., 1998). Zor et al. (2003) observe a large phase at approximately 10 seconds in several of their P-wave receiver functions (most noticeably for stations KRLV and HINS) and suggest, from a grid search inversion technique, that this phase is a multiple from a crustal low velocity zone at roughly 20 km depth.

The east-west profiles also image the lithospheric-asthenospheric boundary (LAB). In section 37° N, the LAB of the northern margin of the Arabian plate (or shield) is clearly visible and indicates that the lithosphere has a thickness of approximately 100 km. In section 38° N, S-to-P converted phases are difficult to interpret and this suggests that the lithospheric structure beneath the Bitlis-Zagros suture zone is very complicated. However, three S-to-P converted phases are identified as LAB signatures: the LAB beneath the Arabian shield for longitudes between 40° and 42° E and depth at roughly 100 km; the LAB beneath the Iranian block (Zagros fold thrust belt) for longitudes between 43° and 45° E and depth of approximately

125 km; and the LAB beneath the EAAC for longitudes between 40° and 43° E and depth ranging between approximately 60 and 85 km.

Both the observed lithosphere beneath the Arabian shield and Iranian block are of typical thickness for continental margins, whereas the lithosphere beneath the EAAC is anomalously thin. The thin lithosphere beneath the EAAC is intimately related to its formation at about 8 Ma when the Tethys oceanic plate detached from the Arabian plate (Şengör et al., 2003). During the initial stages of EAAC development, the mantle lid may not have existed. As the upwelling asthenosphere cooled the thermal boundary layer of the EAAC ($\sim 1280^\circ\text{C}$) would have deepened and so the EAAC would have acquired new lithosphere. A rough estimate of the thickness of the cooled zone below the EAAC using the heat flux equation $D = \sqrt{\kappa t}$, where D is the thickness of cooled lithosphere, $\kappa = 10^{-6}\text{ m}^2/\text{s}$ is the thermal diffusivity typical for rocks and t is the cooling time (from Davies, 1999, page 185), gives minimum and maximum values of 15 and 22 km, for cooling times of 7 and 15 Ma respectively. Therefore, the existence of about 20 km of lithosphere can be explained partly from cooling of the asthenosphere as the thermal boundary layer moved downward. However, this estimate does not preclude the possibility that some lithospheric mantle existed prior to the asthenospheric upwelling.

It is interesting to note the presence of additional strong negative phases in section 38° N for depths between 75 and 125 km which appear to indicate the presence of a laterally extensive and strong upper-mantle structure. However, it is believed that these negative phases are in fact noise and this will be discussed further in section 4.2.

Moving north from the Bitlis-Zagros suture zone, images of the LAB become clearer. In sections 39° and 40° N, the LAB of the EAAC is still anomalously shallow with an average depth of roughly 70 km. In section 39° N the LAB depth mimics the Moho and suggests, for this region of the EAAC, that the crust and mantle lithosphere have deformed coherently. Toward the east, the LAB of the Iranian block is also visible and its location (depth and longitude) is consistent with the neighbouring section 40° N. Furthermore, the LAB depth estimate of 120 km for the Iranian block is similar to the depth estimates from surface wave inversion results for the Central Zagros (Anne Paul, personal communication). In section 40° N, the LAB beneath the EAAC remains shallow and is approximately parallel to the Moho. The lithosphere appears to be very thin at longitude 39° N (region marked by U) and this trend is also visible in the north-south section at 39° E in Figure 5. This area lies geographically in the eastern most part of the Anatolian block where high frequency Sn waves are not observed to propagate (Gök et al., 2003) and where S-wave velocities in the uppermost mantle observed from Rayleigh-wave tomography are low (Sandvol, in prep.). The LAB phase of the EAAC is very weak for longitudes between 41.5° and 43° E (see dotted line in Figure 4). This suggests that either the velocity contrast between the lithosphere and asthenosphere is small possibly due to a small temperature differential or the LAB is in very close proximity to the Moho such that the LAB phases are overshadowed by the Moho phases. The thin lithosphere beneath the Eastern Anatolian block may be related to the deformation within the Anatolian block (i.e., a large pull-apart to the south of the North Anatolian fault). If this interpretation is correct, then local extension involves the entire lithosphere. A region of thickening lithosphere can be seen at longitude 44° N (region marked by D in section 40° N) and could either represent a portion of the lithosphere that has not been as affected by the upwelling hot asthenospheric convection or a portion of the lithosphere beneath the eastern EAAC that is being thickened by the northwesterly convergence of the Iranian plateau. It is interesting to note that this region is associated with an area of high Pn velocities centred at 42° E and 40° N observed by Al-Lazki et al. (2003).

4.2 North-south profiles

Figures 5 through 7 display CCP images of twelve north-south vertical slices for longitudes between 38.5° to 44° E at increments of 0.5°. For longitudes between 38.5° and 41° E (see Figures 5-6), the Moho dips gently from south to north indicating gradual northward crustal thickening in the eastern Anatolian block and western EAAC away from the Arabian margin. The estimated Moho depth, ranging between 30 and 40 km, are similar to those obtained from P-wave receiver functions (Zor et al., 2003). In the eastern sections, the Moho beneath the EAAC and the Iranian block ranges in depth between 40 and 45 km, where the thickest part of the crust is in the central region of the EAAC. The observed Moho depth for the Iranian block is also consistent with those found in Central Iran (Paul et al., 2002, 2003). In Figures 4 and 6-7, it can be seen that the Moho in the central region of the EAAC is sub-horizontal, whereas it is dipping north-east beneath the Anatolian block and western EAAC. The transition from a dipping Moho beneath the Anatolian block to sub-horizontal Moho beneath the EAAC is delineated by the North Anatolian and East Anatolian faults, and reflects the differing deformation styles within these tectonic units.

Similar to the east-west profiles, the UCD also displays the characteristic depth fluctuation as well as regions of weak or non-existent phases. Beneath the eastern Anatolian and Iranian blocks the UCD is not sub-parallel to the Moho, whereas, beneath the EAAC (between 40.5° and 43° E), the UCD and Moho are sub-parallel. The uniform crustal structure of the EAAC indicates that the crust deforms rather uniformly by north-south compression. It should be noted that no UCD phases are observed in section 44° E (see Figure 7) since there is very little ray coverage in this region of the upper crust. The CLVZ observed in the east-west section at 39° N (see Figure 4) is observed in the north-south sections 42° E (see Figure 6). At latitudes greater than 40° N, the southern extent of a CLVZ is imaged in the north-south section 39.5° E. Although there are

volcanic centres within close proximity, the location of this CLVZ is coincident with a geothermal centre south of the Black Sea (see Aydin et al., 2005, Figure 2).

The LAB signature of the Anatolian block is imaged in sections 39° to 39.5° E (see Figure 5) with depth ranging between 75 and 85 km. As the Anatolian block pinches out eastward, where the North Anatolian and East Anatolian faults meet at the Karliova triple junction, the images of the LAB of the Arabian block (see Figures 5 and 6) become less coherent due to complexities associated with the Bitlis–Zagros suture zone and the western EAAC. Also imaged is the LAB of the Rhodope–Pontides fragment which could represent a continuous northern extension of the LAB of the EAAC. However, due to the severe crustal fragmentation within this region it is likely that the lithosphere below the Rhodope–Pontides is distinct from that of the EAAC. In sections 39° E to 44° E, the LAB of the EAAC is relatively consistent throughout with an average depth of about 70 km. The minimum depth of approximately 65 km in section 39° E (“U” at latitude 40° N in Figure 5) matches that of the east–west section 40° N (longitude 39° E in Figure 4). The LAB signal is weak below the central EAAC between 39° and 40° N and this correlates well with the location of Quaternary volcanoes and shallowest Curie–point depths (Aydin et al., 2005).

The presence of the strong negative phases appearing at depths between 75 and 125 km in the EW section 38° N and in the NS sections between 37° and 39° N is believed to be caused by several factors. To explore these factors, it is best to consider a hypothetical cross–section with a N–S orientation perpendicular to the sections in Figure 4. Figure 8 is a cartoon representation of the crust and mantle for a north–south profile bisecting the Bitlis suture zone. Due to the tectonically complex geometry of the region, it is expected that the two– and three–dimensional structure of the lithosphere below the Bitlis–Zagros suture (e.g., truncation and inter–fingering of delaminated lithospheres) will introduce wavefront diffractive and scattering effects. Also, below the Bitlis suture in the south–west, Rayleigh wave tomography has imaged an extensive zone of low shear wave velocity (Sandvol, in prep.). This region of partially melted mantle may be acting as a lens by focusing or de–focusing upcoming teleseismic energy. Since the CCP imaging method cannot transform these diffractive effects properly into the offset and depth space correctly (Wilson et al., 2003), the images will suffer from improper migration of these artifacts. Furthermore, since the EAAC was devoid of any old lithospheric root and was predominantly supported by subducted oceanic slab prior to slab detachment (Keskin, 2005) it is possible that any remaining subducted oceanic lithosphere has a lower crust component. For such a scenario, a velocity discontinuity would exist where the oceanic crust abuts the thin lithosphere of the EAAC (see LLB in Figure 8). This may also help explain the strong negative phase observed above the LAB signature for the Iranian block for longitudes between 43° and 45° E in east–west section 40° N (see Figure 4). It is possible that a compositional contrast also exist from serpentinization of the oceanic lithosphere, although this contrast may not have a sufficient enough gradient. There would be no significant compositional contrast expected for continental–continental lithospheric boundaries, such as the boundary between the top of the Arabian lithosphere and bottom of the subducted oceanic lithosphere. A wet oceanic lithosphere would also help explain the presence of partially melted lithosphere within this region, where the escape of water from the subducted oceanic lithosphere and crust would lower the solidus of the mantle.

Although the Bitlis–Zagros suture introduces complexity into the receiver function images of the LAB for latitudes between 37° and 39° N (see dotted ellipses in Figures 4–6), it is conceivable that the LAB of the Arabian shield and the Iranian block are being delineated. In sections 40° to 42° E (see Figures 5–6), the lithospheric thickness of the Arabian margin thins from approximately 125 km to 100 km as the north–south profiles sample less of the interior shield and more of the Bitlis–Zagros suture zone. The lithosphere of the Iranian block ranges in thickness between 90 and 120 km (sections 42.5° to 44° E in Figure 7).

5 CONCLUSIONS

A simplified interpretation of the crustal and upper–mantle structure of eastern Turkey is shown in Figures 9 and 10. The crust has an average depth of approximately 45 km, thickening from west to east and south to north, and compares well with the P–wave receiver results of Zor et al. (2003), although not exactly. The upper–crustal discontinuity at roughly 10 km depth is likely associated with volcano–sedimentary successions and the crustal low velocity zones at depths of 25 km are consistent with the location of geothermal and Quaternary volcanic centres. Beneath the EAAC, where the crust is thickest, the UCD and the Moho discontinuities are sub–parallel and this indicates that deformation is vertically uniform. The LAB for the EAAC is anomalously thin with an average depth of approximately 70 km. The observation that the lithosphere is shallow below EAAC supports the idea that the tectonically–deformed domal structure (see top plots in Figures 9 and 10) is supported by an asthenospheric upwelling. Thus the fact that the crust is thickest and uniform below the EAAC is plausible since this region is hot and weak. The LAB for the Arabian shield and Iranian block have depths of approximately 100 to 125 km typical of continental margins. Furthermore, the LAB of the Arabian shield does not appear to underthrust eastern Turkey and this is consistent with the oceanic slab breakoff model of Keskin (2003).

Although the imaged depths of the crustal and upper–mantle seismic discontinuities are within range of those estimated from previously published results, it should be stressed that our S–wave receiver function depths are calculated based on a

1-D velocity model from Rayleigh-wave tomography. To examine the effect of using this 1-D velocity model, we reanalysed the data using several other 1-D crustal and upper-mantle velocity models developed for this region (i.e., Çakir et al. (2004) and Kaypak et al. (2004)). Our tests indicated that the geometry remained relatively unchanged (at least to first-order) and only the depth estimates varied, as was expected. Even within the estimated depth error bounds, our results strongly indicate that in eastern Turkey the crust has not experienced significant thickening and the lithosphere is anomalously thin below the EAAC.

It is interesting to note that the LAB of the EAAC and the Anatolian, Iranian, and the Rhodope-Pontide blocks appear to be distinctly imaged. This would suggest that eastern Turkey is indeed melange of several lithospheric fragments. Since the spatial resolution of the S-wave receiver function is on the order of 10 km and due to the large station spacing, it is difficult to observe whether the crust also shows similar fragmentation. Therefore it is not possible to determine whether the faults extend deep into the lower crust, as would be expected for a region composed of several crustal blocks, or whether deformation is distributed throughout the crust with no Moho offset (e.g., Wilson et al., 2004).

The main point of practical significance is that the S-wave receiver function profiles demonstrate an upper-mantle geometry consistent with the 'oceanic slab steepening and break off' model of Keskin (2003). The existence of a low velocity mantle beneath the EAAC has been established (e.g., Kadinsky-Cade et al., 1981; Hearn & Ni, 1994; Gök et al., 2000), but the nature of the lithosphere and detailed crustal structure of the EAAC and surrounding region are not well known. It has been suggested that the asthenosphere was in contact with the crust of the EAAC since slab breakoff at about 8 Ma (Şengör et al., 2003). Our observation show with good resolution the existence of clear LAB below the EAAC within the depth range of 60 and 80 km, where late Miocene to recent volcanism is significant.

ACKNOWLEDGMENTS

The authors would like to thank Prakash Kumar, Rainer Kind, Forough Sodoudi and others at GFZ Potsdam, Mehmet Keskin, and Boris Kiefer for providing valuable discussions during this research. Constructive review by Thomas Hearn improved this paper. We would like to thank the two anonymous reviewers for their helpful and constructive comments. This research is supported by the Continental Dynamic program and Geophysics Program of the U.S. National Science Foundation under grants EAR9614616 and EAR0335802.

References

- Al-Damegh, K., Sandvol, E., Al-Lazki, A. & Barazangi, M., 2004. Regional seismic wave propagation (Lg and Sn) and Pn attenuation in the Arabian plate and surrounding regions, *Geophys. J. Int.*, **157**, 775–795.
- Al-Lazki, A. I., Seger, D., Sandvol, E., Türkelli, N., Mohamad, R. & Barazangi, M., 2003. Tomographic Pn velocity and anisotropy structure beneath the Anatolian plateau (eastern Turkey) and the surrounding regions, *Geophys. Res. Lett.*, **30**(24), 8043, doi:10.1029/2003GL017391.
- Ates, A., Kearey, P. & Tufan, S., 1999. New gravity and magnetic anomaly maps of Turkey, *Geophys. J. Int.*, **136**, 499–502.
- Aydin, İ., Karat, H. İ & Koçak, A., 2005. Curie-point depth map of Turkey, *Geophys. J. Int.*, **162**, 633–640.
- Bachmanov, D.M., Trifonov, V.G., Hessami, Kh.T., Kozhurin, A.I., Ivanova, T.P., Rogozhin, E.A., Hademi, M.C. & Jamali, F.H., 2004. Active faults in the Zagros and central Iran, *Tectonophysics*, **380**, 221–241.
- Barazangi, M., Sandvol, E. & Seber, D., 2005. Structure and tectonic evolution of the Anatolian plateau in eastern Turkey, *GSA Today*, in press.
- Bock, G., 1988. Sp phases from the Australian upper mantle, *Geophys. J.*, **94**, 73–81.
- Bock, G., 1991. Long-period S to P converted waves and the onset of partial melting beneath Oahu, Hawaii, *Geophys. Res. Lett.*, **18**, 869–872.
- Bock, G. & Kind, R., 1991. A global study of S-to-P and P-to-S conversions from the upper mantle transition zone, *Geophys. J. Int.*, **107**, 117–129.
- Bozkurt, E., 2001. Neotectonics of Turkey: a synthesis, *Geodinamica Acta*, **14**, 3–30.
- Bozkurt, E., & Mittwede, S., 2001. Introduction to the geology of Turkey – a synthesis, *International Geology Review*, **43**, 578–594.
- Bostock, M.G. & Rondenay, S., 1999. Migration of scattered teleseismic body waves, *Geophys. J. Int.*, **137**, 732–746.
- Burke, K. & Şengör, C., 1987. Regional lineaments and continental evolution, *Regional geophysical lineaments; their tectonic and economic significance Memoir*, Geological Society of India, **12**, 65–73.
- Çakir, Ö., Erduran, M., Çınar, H., & Yilmaztürk, A., 2000. Forward modelling receiver functions for crustal structure beneath station TBZ (Trabzon, Turkey), *Geophys. J. Int.*, **140**, 341–356.
- Çakir, Ö. & Erduran, M., 2004. Constraining crustal and uppermost mantle structure beneath station TBZ (Trabzon, Turkey) by receiver function and dispersion analyses, *Geophys. J. Int.*, **158**, 955–971.
- Davies, G. F., 1999. *Dynamic Earth: Plates, Plumes and Mantle Convection*, Cambridge University Press, Cambridge, UK.
- Dewey, J.F., Hempton, M.R., Kidd, W.S.F., Saroglu, F., & Şengör, A.M.C., 1986. Shortening of continental lithosphere: The neotectonics of Eastern Anatolia – a young collision zone, *Collision Tectonics, Geological Society Special Publication*, **19**, 3–36.
- Dueker, K. G. & Sheehan, A. F., 1998. Mantle discontinuity structure beneath the Colorado Rocky Mountains and High Plains, *J. Geophys. Res.*, **103**, 7153–7169.
- Farra, V. & Vinnik, L., 2000. Upper mantle stratification by P and S receiver functions, *Geophys. J. Int.*, **141**, 699–712.

- Gök, R., Sandvol, E., Tükkelli, N., Seber, D. & Barazangi, M., 2003. Sn attenuation in the Anatolian and Iranian plateau and surrounding regions, *Geophys. Res. Lett.*, **30**(24), 8042, doi:10.1029/2003GL018020.
- Gök, R., Tükkelli, N., Sandvol, E., Seber, D. & Barazangi, M., 2000. Regional wave propagation in Turkey and surrounding regions, *Geophys. Res. Lett.*, **27**(3), 429–432.
- Hatzfeld, D., Tatar, M., Priestley, K. & Ghafory-Ashtiany, M., 2003. Seismological constraints on the crustal structure beneath the Zagros Mountain belt (Iran), *Geophys. J. Int.*, **155**, 403–410.
- Hearn, T.M. & Ni, J.F., 1994. Pn velocities beneath continental collision zones: the Turkish–Iranian Plateau, *Geophys. J. Int.*, **117**, 273–283.
- Jiménez-Munt, I., Sabadini, R., & Gardi, A., 2003. Active deformation in the Mediterranean from Gibraltar to Anatolia inferred from numerical modeling and geodetic and seismological data, *J. Geophys. Res.*, **108**(B1), 2006, doi:10.1029/2001JB001544.
- Jordan, T.H. & Frazer, L.N., 1975. Crustal and upper mantle structure from Sp Phases, *J. geophys. Res.*, **80**, 1504–1518.
- Kadinsky-Cade, K., Barazangi, M., Oliver, J. & Isacks, B., 1981. Lateral variation in high-frequency seismic wave propagation at regional distances across the Turkish and Iranian plateaus, *J. Geophys. Res.*, **86**, 9377–9396.
- Karig, D.E. & Kozlu, H., 1990. Late Paleogene Neogene evolution of the triple junction region near Maras, south-central Turkey, *J. Geol. Soc.*, **147**(6), 1023–1034.
- Kaypak, B. & Eyidoğan, H., 2004. One-dimensional crustal structure of the Erzincan basin, Eastern Turkey and relocations of the 1992 Erzincan earthquake (Ms=6.8) aftershock sequence, *Phys. Earth planet. Int.*, **151**(1–2), 1–20, 10.1016/j.pepi.2004.11.009.
- Keskin, M., 2003. Magma generation by slab steepening and breakoff beneath a subduction–accretion complex: An alternative model for collision-related volcanism in Eastern Anatolia, Turkey, *Geophys. Res. Lett.*, **30**(24), 8046, doi:10.1029/2003GL018019.
- Keskin, M., 2005. Domal uplift and volcanism in a collision zone without a mantle plume: Evidence from Eastern Anatolia, www.MantlePlumes.org.
- Keskin, M., Pearch, J.A. & Mitchell, J.G., 1998. Volcano–stratigraphy and geochemistry of collision-related volcanism on the Erzurum–Kars Plateau, northeastern Turkey, *J. Volcanol. Geotherm. Res.*, **85**, 355–404.
- Koçyiğit, A., Yilmaz, A., Adamia, S. & Kuloshvili, S., 2001. Neotectonics of East Anatolian Plateau (Turkey) and Lesser Caucasus: implications for transition from thrusting to strike–slip faulting, *Geodinamica Acta*, **14**, 177–195.
- Kumar, P., Yuan, X., Kind, R. & Kosarev, G., 2005. The Lithosphere–Asthenosphere boundary in the Tien Shan–Karakoram region from S receiver functions – Evidence of continental subduction, *Geophys. Res. Lett.*, **32**, L07305.
- Li, X., Kind, R., Yuan, X., Wölber, I. & Hanka, W., 2004. Rejuvenation of the lithosphere by the Hawaiian plume, *Nature*, **427**, 827–829.
- Maggi, A. & Priestley, K., 2005. Surface waveform tomography of the Turkish–Iranian plateau, *Geophys. J. Int.*, **160**, 1068–1080.
- Meier, T., Dietrich, K., Stöckhert, B., & Harjes, H.–P., 2004. One-dimensional models of shear wave velocity for the eastern Mediterranean obtained from the inversion of Rayleigh wave phase velocities and tectonic implications, *Geophys. J. Int.*, **156**, 45–58.
- Mohsen, A., Hofstetter, R., Bock, G., Kind, R., Weber, M., Wylegalla, K., Rumpker, G. & the DESERT Group, 2005. A receiver study across the Dead Sea Transform, *Geophys. J. Int.*, **160**, 948–960.
- Örgülü, G., Aktar, M., Türkelli, N., Sandvol, E., & Barazangi, M., 2003. Contribution to the seismotectonics of Eastern Turkey from moderate and small size events, *Geophys. Res. Lett.*, **30**(24), 8040, doi:10.1029/2003GL018258.
- Paul, A., Kaviani, A., Vergne, J., Hatzfeld, D. & Mokhtari, M., 2002. First seismological data on the crustal structure of the Zagros, *Eos Trans., AGU*, **83**(47).
- Paul, A., Kaviani, A., Hatzfeld, D. & Mokhtari, M., 2003. Lithospheric structure of central Zagros from seismological tomography, *Fourth International Conference Earthquake Engineering and Seismology*, 12–14 May, 2003, Tehran, Islamic Republic of Iran.
- Pearce, J.A., Bender, J.F., De Long, S.E., Kidd, W.S.F., Low, P.J., Guner, Y., Saroglu, F., Yilmaz, Y., Moorbath, S. & Mitchell, J.G., 1990. Genesis of collision volcanism in Eastern Anatolia, Turkey, *J. Volcanol. Geotherm. Res.*, **44**, 189–229.
- Reilinger, R.E., McClusky, S.C., Oral, M.B., King, R.W., Toksoz, M.N., Barka, A.A., Kinik, I., Lenk, O. & Sanli, I., 1997. Global positioning system measurements of present-day crustal movements in the Arabia–Africa–Eurasia plate collision zone, *J. Geophys. Res.*, **102**(B5), 9983–9999.
- Reilinger, R.E., McClusky, S.C., Souter, B.J., Hamburger, M.W., Prilepin, M.T., Mishin, A., Guseva, T. & Balassanian, S., 1997. Preliminary estimates of plate convergence in the Caucasus collision zone from global positioning system measurements, *Geophys. Res. Lett.*, **24**(14), 1815–1818.
- Rodgers, A.J, Ni, J.F. & Hearn, T.M., 1997. Propagation characteristics of short-period Sn and Lg in the Middle East, *B.S.S.A.*, **87**, 396–413.
- Saintot, A. & Angelier, J., 2002. Tectonic paleostress fields and structural evolution of the NW–Caucasus fold-and-thrust belt from Late Cretaceous to Quaternary, *Tectonophysics*, **357**, 1–31.
- Sandvol, E., Türkelli, N., & Barazangi, M., 2003a. The Eastern Turkey Seismic Experiment: The study of a young continent–continent collision, *Geophys. Res. Lett.*, **30**(24), 8038, doi:10.1029/2003GL018192.
- Sandvol, E., Türkelli, N., Zor, E., Gök, R., Bekler, T., Gürbüz, C., Seber, D., & Barazangi, M., 2003b. Shear wave splitting in a young continent–continent collision: An example from Eastern Turkey, *Geophys. Res. Lett.*, **30**(24), 8041, doi:10.1029/2003GL017390.
- Sandvol, E., 2004. The seismic structure of the Eurasian–Arabian collisional belt, *Abstracts with Programs – Geological Society of America*, **36**(5), 48.
- Sandvol, E. & Zor, E., 2004. Upper mantle P and S-wave velocity structure beneath eastern Anatolian plateau, *Eos (Transactions, American Geophysical Union)*, AGU Fall Meeting 2004, S13B–1056.
- Sandvol, R., in prep.. Rayleigh wave tomography of Eastern Turkey,
- Şengör, A.M.C. & Kidd, W.S.F., 1979. The post-collisional tectonics of the Turkish–Iranian Plateau and a comparison with Tibet, *Tectonophysics*, **55**, 361–376.
- Şengör, A.M.C. & Yilmaz, Y., 1981. Tethyan evolution of Turkey: A plate tectonic approach, *Tectonophysics*, **75**, 181–241.
- Şengör, A.M.C. & Natalin, B.A., 1996. Turcic-type orogeny and its role in the making of the continental crust, *Ann. Rev. Earth Plan. Sci.*, **24**, 263–337.
- Şengör, A. M. C., Özeren, S., Genç, T. & Zor, E., 2003. East Anatolian high plateau as a mantle-supported, north–south shortened domal structure, *Geophys. Res. Lett.*, **30**(24), 8045, doi:10.1029/2003GL017858.

- Türkelli, N., Sandvol, E., Zor, E., Gök, R., Bekler, T., Al-Lazki, A., Karaabulut, H., Kuleli, S., Eken, T., Gürbüz, C., Bayraktutan, S., Deber, D. & Barazangi, M., 2003. Seismogenic zones in Eastern Turkey, *Geophys. Res. Lett.*, **30**(24), 8039, doi:10.1029/2003GL018023.
- Türkelli, N., 2004. Lithospheric structure in eastern Turkey, *Abstracts with Programs – Geological Society of America*, **36**(5), 51–52.
- Wilson, C. K., Jones, C. H., Molnar, P., Sheehan, A. F. & Boyd, O. S., 2004. Distributed deformation in the lower crust and upper mantle beneath a continental strike–slip fault zone: Marlborough fault system, South Island, New Zealand, *Geology*, **32**(10), 837–840.
- Wilson, D.C., Angus, D.A., Ni, J. & Grand, S., in press, Constraints on the interpretation of S-to-P receiver functions, *Geophys. J. Int.*
- Wilson, D. & Aster, R., 2005. Seismic imaging of the crust and upper mantle using regularized joint receiver functions, frequency–wave number filtering, and multimode Kirchhoff migration, *J. Geophys. Res.*, **110**(B05305), doi:10.1029/2004JB003430.
- Wilson, D., Aster, R., & the RISTRA Group, 2003. Imaging crust and upper mantle seismic structure in the southwestern United States using teleseismic receiver functions, *The Leading Edge*, **22**, 232–237.
- Yilmaz, Y., 1993. New evidence and model on the evolution of the southeast Anatolian orogen, *Geological Society of America Bulletin*, **105**, 251–271.
- Zor, E., Sandvol, E., Gürbüz, C., Türkelli, N., Seber, D. & Barazangi, M., 2003. The crustal structure of the East Anatolian plateau (Turkey) from receiver functions, *Geophys. Res. Lett.*, **30**(24), 8044, doi:10.1029/2003GL018192.

Figure Captions

Figure 1. A simplified tectonic map of Anatolia and the northern Middle East showing Holocene volcanoes (triangles), active thrust faults (barbed lines) and active strike slip faults (plain lines). Abbreviations: LC – Lesser Caucasus; GC – Greater Caucasus; BS – Bitlis Suture; ZS – Zagros Suture; EAF – East Anatolian Fault; NAF – North Anatolian Fault; DSF – Dead Sea Fault. The area of study for the S–wave receiver function analysis is enclosed by the dashed rectangle.

Figure 2. Map showing the location of the 29 three–component PASSCAL broadband stations in the ETSE array (inverted triangles), the two permanent stations GNI (GSN–IRIS/USGS network) and MALT (GEOFON network) (triangles) and Holocene volcanoes (circles). Abbreviations: NAF, North Anatolian Fault; EAF, East Anatolian Fault; BZS, Bitlis–Zagros Suture Zone. Approximate location of the major tectonic units of eastern Turkey are shown (modified from Keskin, 2005): (I) Rhodope–Pontide fragment, (II) Northwest Iranian fragment, (III) Eastern Anatolian Accretionary complex (EAAC), (IV) Bitlis–Poturge Massif, and (V) Arabian foreland.

Figure 3. Global distribution of the 81 events used in the S–wave receiver function study.

Figure 4. East–west profiles at 37°, 38°, 39° and 40° N. In this and the remaining figures, the dashed lines are the inferred seismic discontinuities for the crust and upper mantle. The dotted lines indicate regions where the LAB is very weak. The dotted ellipse, in this and the remaining figures, highlights the region where the Bitlis–Zagros suture zone (BZSZ) is believed to introduce complexity in the receiver function images. A dashed–dotted ellipse indicates a crustal low velocity zone (CLVZ). The letter **U** highlights a region of thin lithosphere (also seen in Figure 5) and the letter **D** a region of thick lithosphere. Abbreviations: UCD, upper–crust discontinuity; LAB, lithosphere–asthenosphere boundary; EAAC, East Anatolian accretionary complex; AS, Arabian Shield; IB, Iranian Block. The location where the vertical profile crosses a major fault zone is indicated along the top. Note: straight lines in figures 4–7 do not indicate missing signal, but rather lack of data.

Figure 5. North–south profiles at 38.5°, 39°, 39.5° and 40° N. The LAB (RP), Rhodope–Pontide continental fragment (or block), may or may not be a thickened continuation of the EAAC LAB to the south.

Figure 6. North–south profiles at 40.5°, 41°, 41.5° and 42° N.

Figure 7. North–South profiles at 42.5°, 43°, 43.5° and 44° N.

Figure 8. Schematic diagram showing splaying of oceanic and continental lithosphere, regions where teleseismic energy is diffracted and scattered, and possible lithosphere–lithosphere boundary (LLB) due to the presence of subducted oceanic crust.

Figure 9. Top: Topographic relief of eastern Turkey at 39° N. Bottom: sketch illustrating the collision of the Arabian and Eurasian plates summarizing the results of S–receiver function analysis for an east–west cross section at 39° N.

Figure 10. Top: Topographic relief of eastern Turkey at 42° E. Bottom: sketch illustrating the collision of the Arabian and Eurasian plates summarizing the results of S–receiver function analysis for a north–south cross section at 42° E.

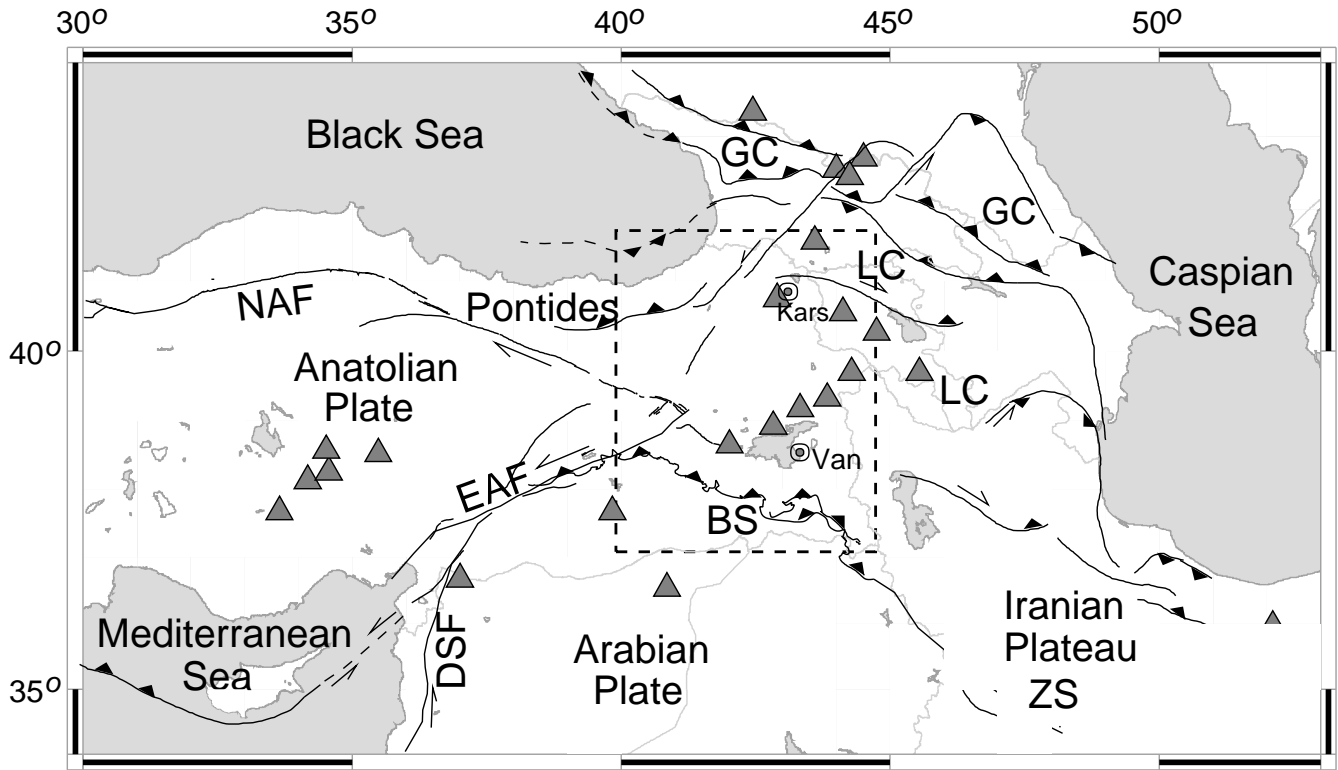


Figure 1.

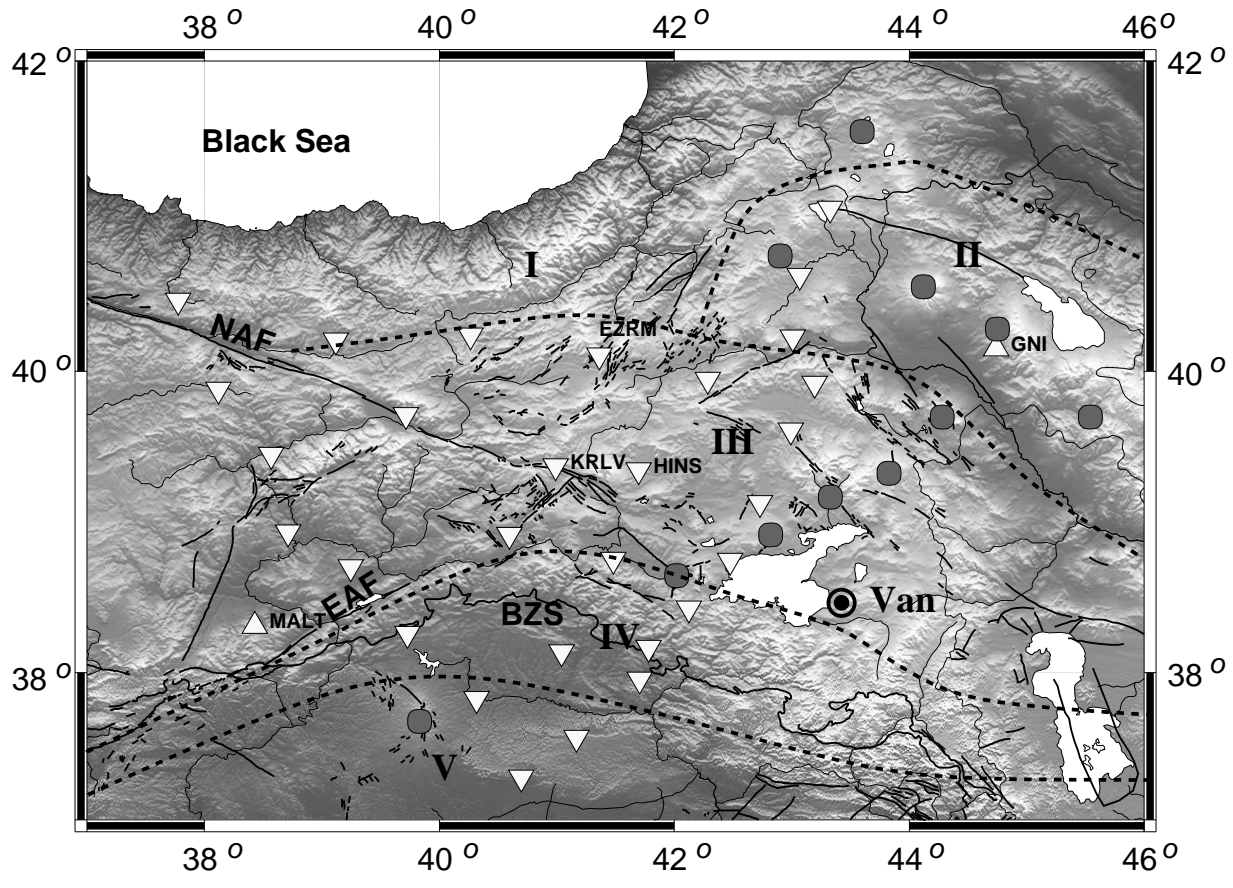


Figure 2.

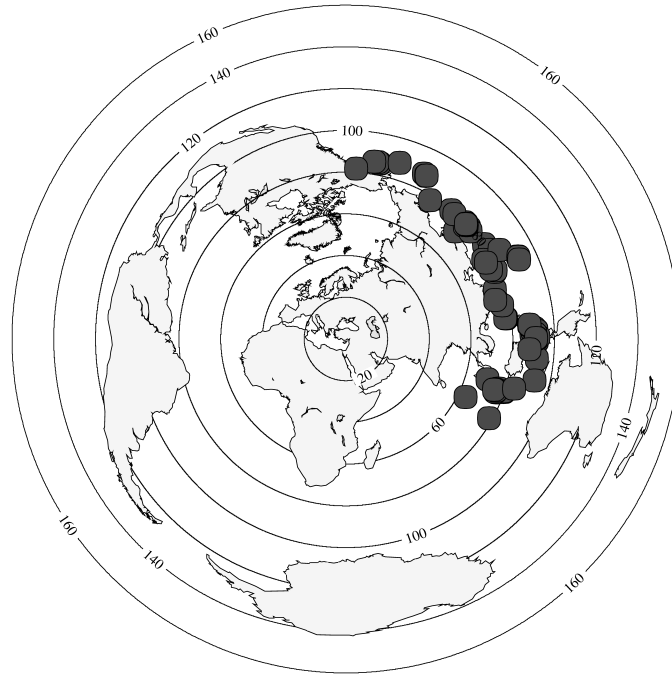


Figure 3.

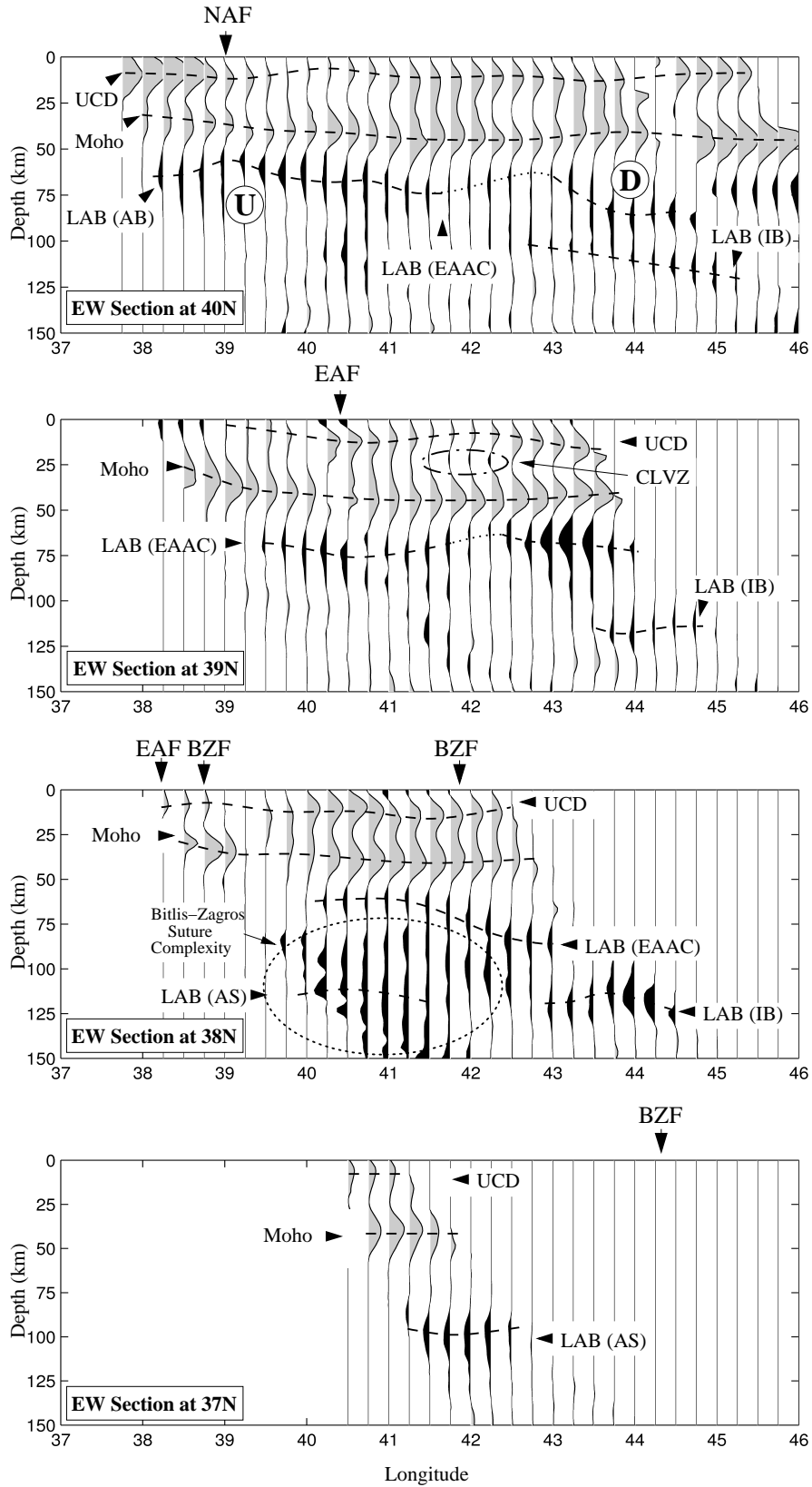


Figure 4.

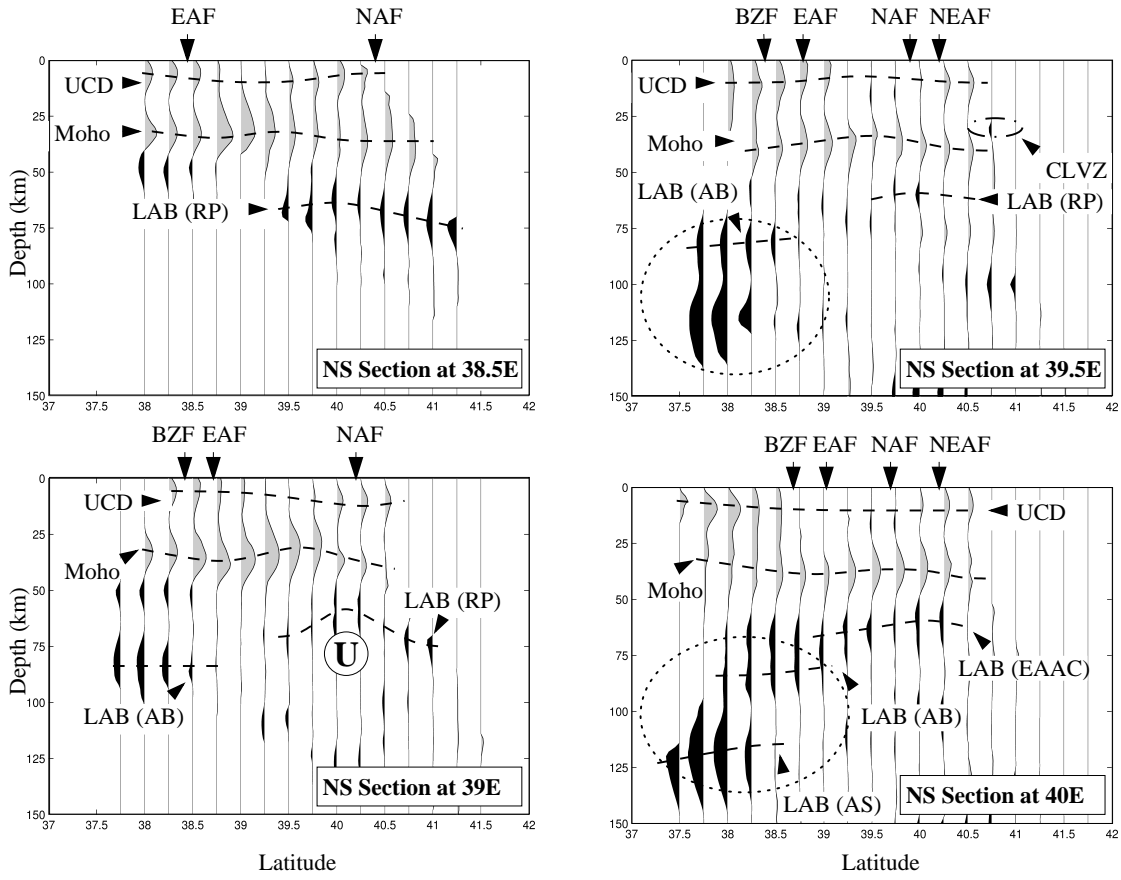


Figure 5.

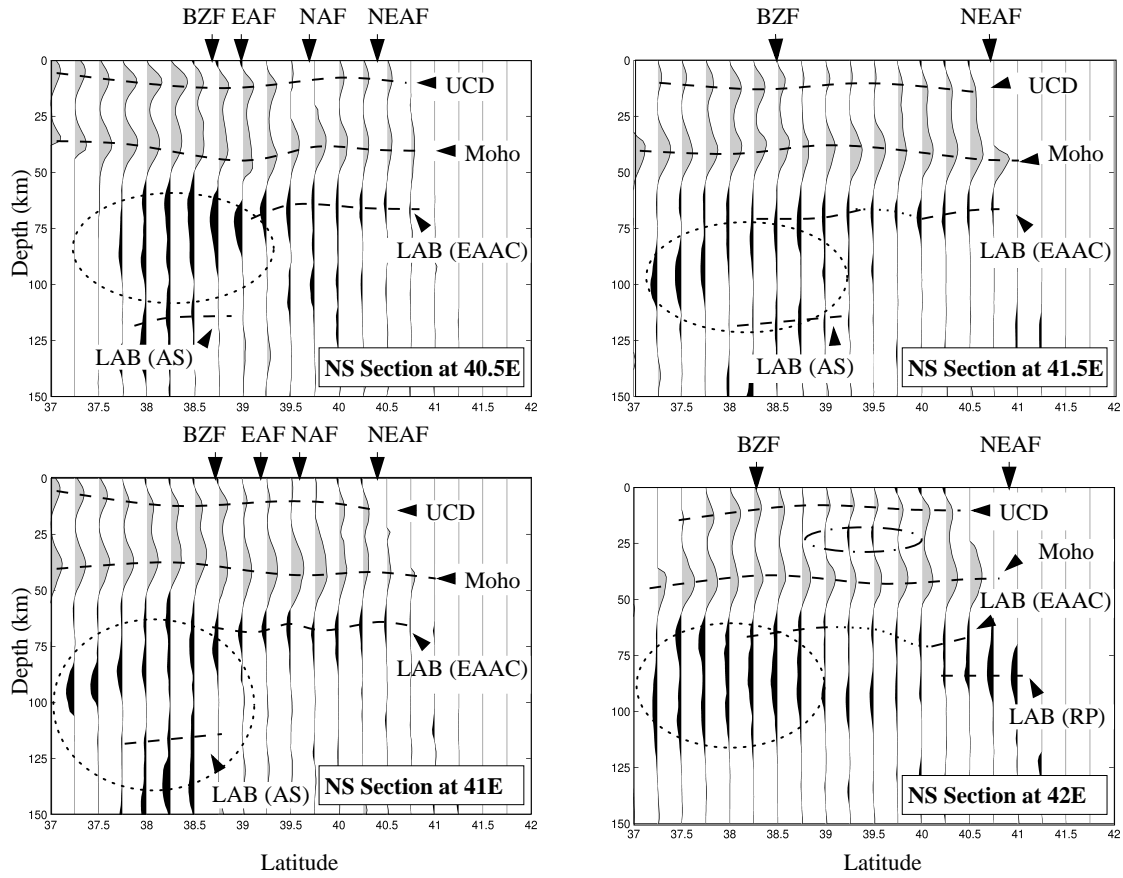


Figure 6.

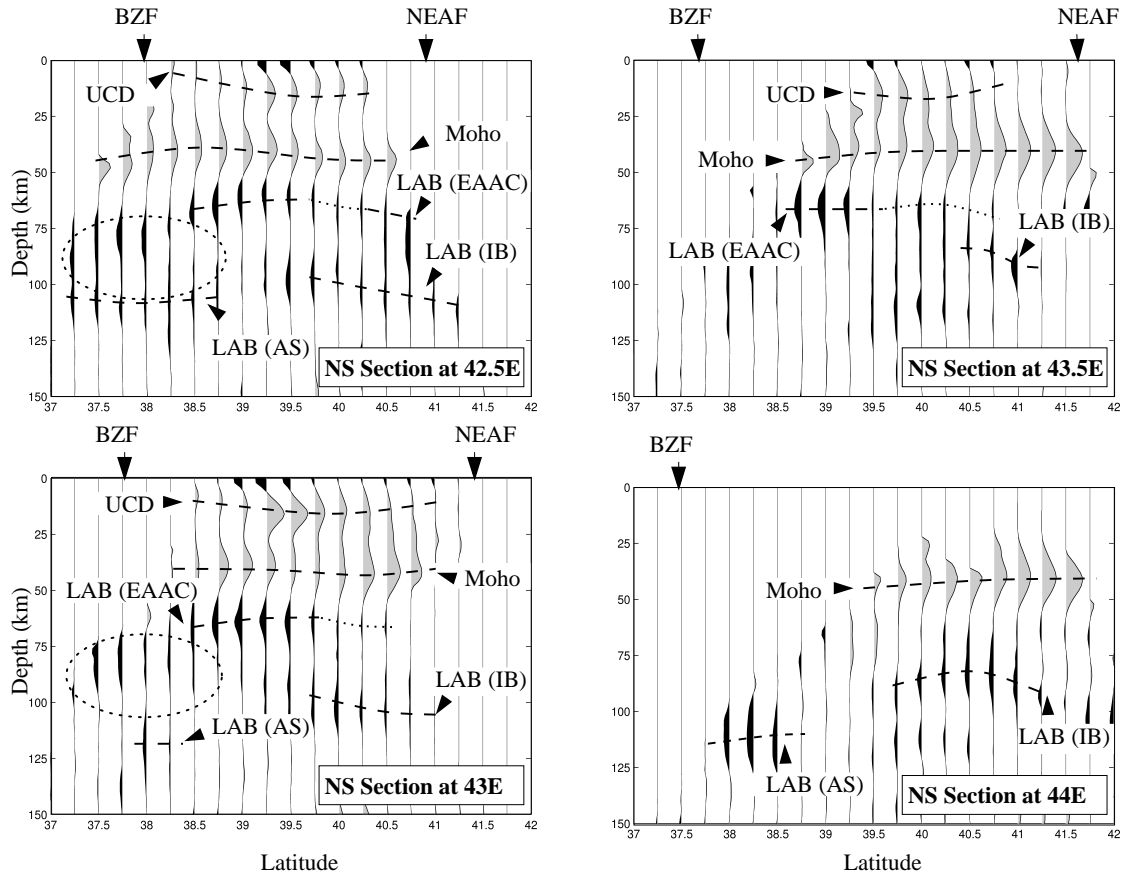


Figure 7.

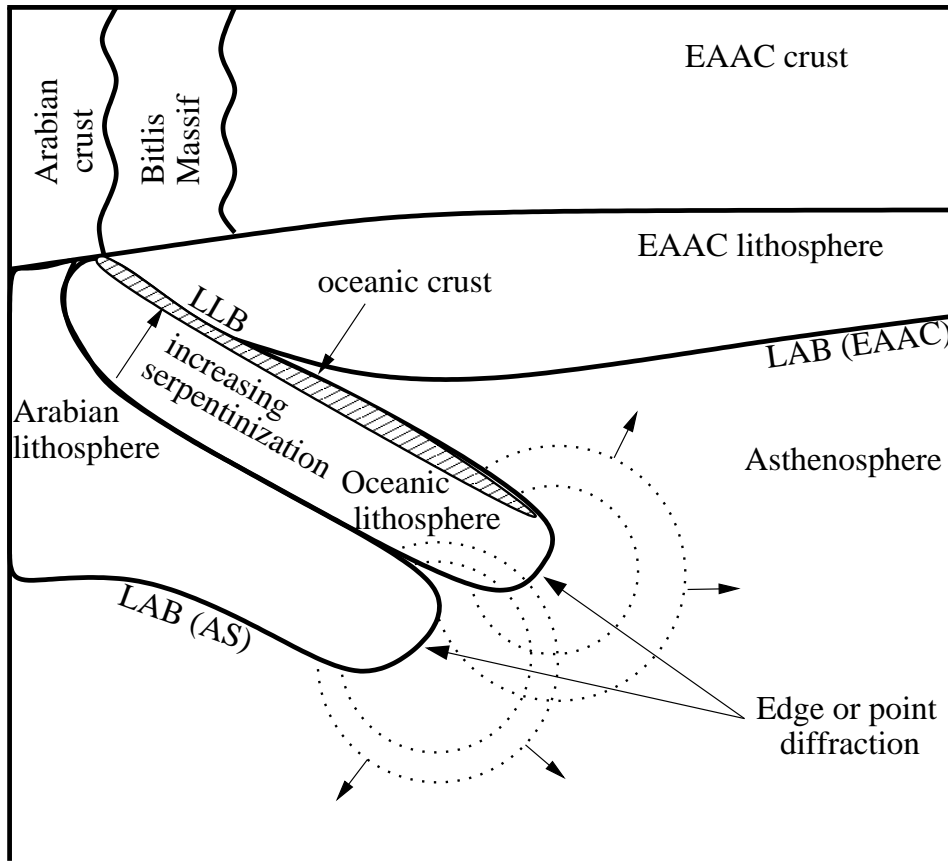


Figure 8.

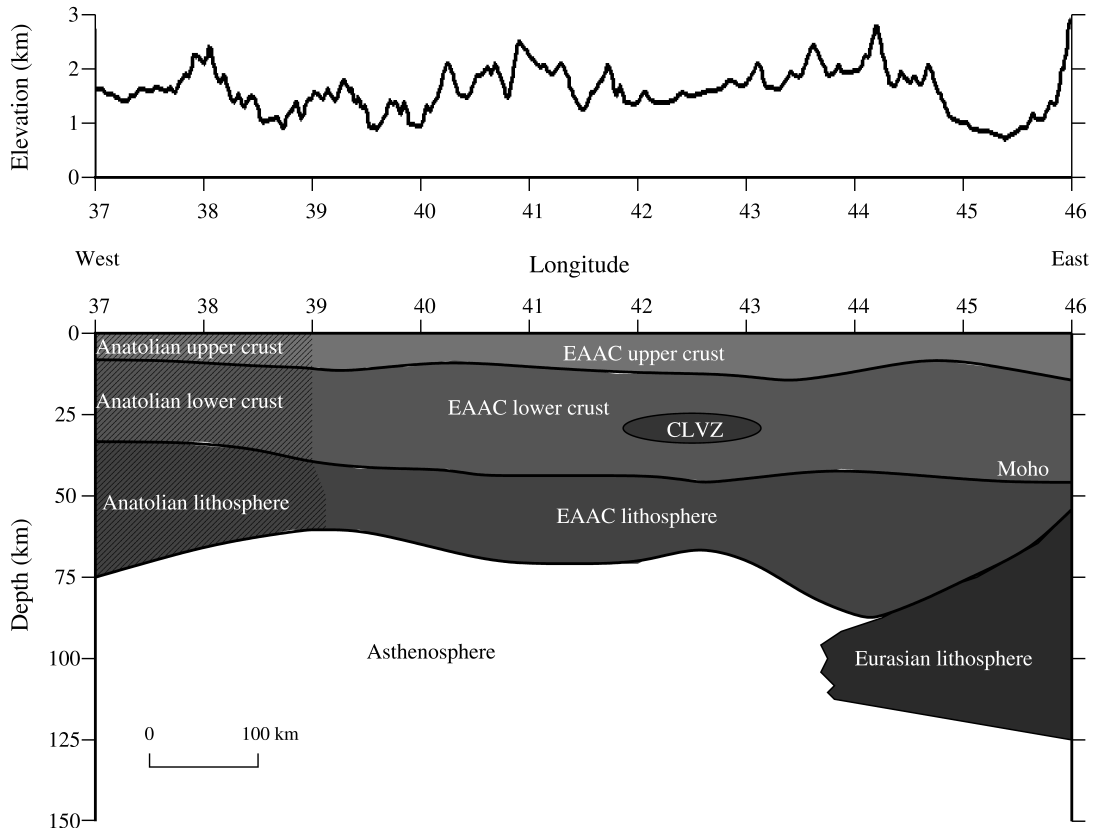


Figure 9.

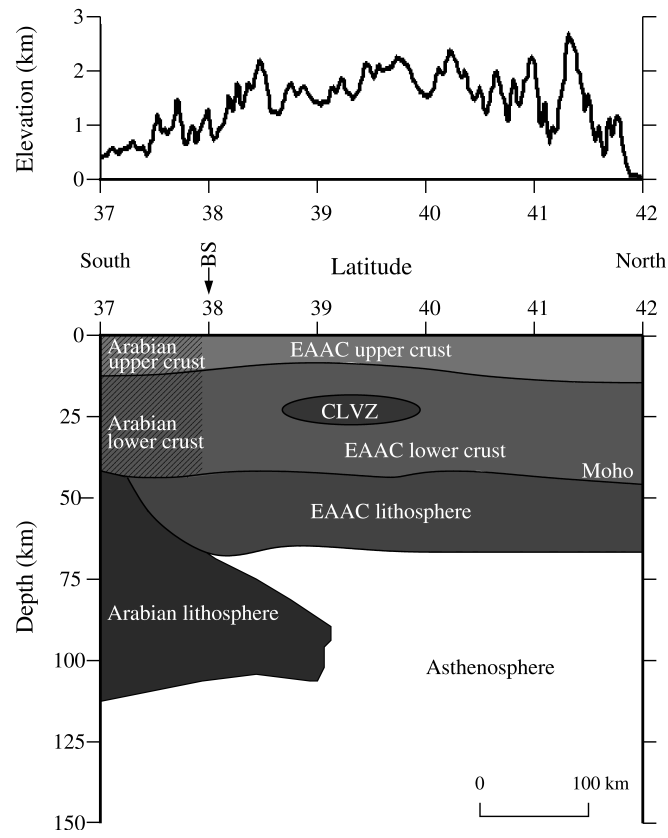


Figure 10.